

Solid Mesh Registration for Radiotherapy Treatment Planning

Karsten Østergaard Noe^{1,3} and Thomas Sangild Sørensen^{1,2}

¹ Department of Computer Science, Aarhus University, Denmark
`noe@cs.au.dk`

² Institute of Clinical Medicine, Aarhus University, Denmark

³ The Alexandra Institute, Denmark

Abstract. We present an algorithm for solid organ registration of pre-segmented data represented as tetrahedral meshes. Registration of the organ surface is driven by force terms based on a distance field representation of the source and reference shapes. Registration of internal morphology is achieved using a non-linear elastic finite element model. A key feature of the method is that the user does not need to specify boundary conditions (surface point correspondences) prior to the finite element analysis. Instead the boundary matches are found as an integrated part of the analysis. The method is evaluated on phantom data and prostate data obtained in vivo based on fiducial marker accuracy and inverse consistency of transformations. The parallel nature of the method allows an efficient implementation on a GPU and as a result the method is very fast. All validation registrations take less than 30 seconds to complete. The proposed method has many potential uses in image guided radiotherapy (IGRT) which relies on registration to account for organ deformation between treatment sessions.

1 Introduction

The challenge of registering solid organs to a common reference configuration is often encountered in medical image computing applications. In image guided radiotherapy (IGRT) for example, optimal conformation of radiation dose to tumour tissue is directly linked to the ability to adapt dose delivery to morphological variations encountered during repeated treatment sessions. Accurate conformation is of utmost importance since radiation of healthy tissue may induce severe side effects. On the other hand, failing to deliver a sufficient dose to the tumour results in failure to kill all cancer cells. Ideally organ deformations during and between treatments should be taken into account based on repetitive 3D image acquisitions (CT, CBCT, MRI etc.). By registering the corresponding organs to a common reference configuration, a geometrically resolved view can be obtained and used e.g. to compute the accumulated dose delivered at any given physical point and adjust the treatment plan accordingly.

Due to organ delineation necessary for radiotherapy treatment planning it is in many cases fair to assume that organs have been segmented prior to registration.

Having segmented an organ in two configurations however does not imply that a correct surface correspondence function is defined, let alone correspondence of interior morphology. This paper describes an automatic algorithm to register two solid meshes (tetrahedral meshes in the current work), which does not require the user to specify boundary correspondences. The algorithm computes a transformation, which maps boundary nodes in the source mesh onto the boundary of the reference mesh subject to a minimisation of the elastic energy interiorly in the deformed source mesh. The algorithm iteratively deforms the source mesh towards the reference mesh. In each iteration and for each node near the source mesh's surface, a force acting on the corresponding node is computed. This force expression is derived from Euclidean distance field computations and mesh in-trinsics. Based on these driving forces a non-linear elastic finite element model (FEM) subsequently computes node displacements for the entire source mesh. The presented work is the continuation of work previously published [1] in which we used a simpler elastic model [2] for regularisation of the organ deformation.

2 Related Work

Since using distance fields and finite element analysis (FEA) for mesh registration is not unique to this paper we reference some representative previous work in the following.

Some authors have used elastic FEA as a regularisation term in intensity based registration. In [3] a linear elastic deformable FEM is applied to the entire image domain, and the image is divided into subvolumes, which are given different material properties. These are connected by appropriate boundary conditions. This technique is used for registering images used in preoperative planning of brain surgery. In subsequent work the linear elastic model is coupled with a model of incompressible fluids via appropriate boundary conditions [4]. Peckar et al. have used linear elastic FEA for finding a smooth transformation that satisfies a number of point constraints. Schnabel et al. [5] have also used a finite element model in connection with intensity based registration, but for creation of images to be registered; their idea was to generate realistic registration problems with a known displacement mapping to evaluate the accuracy of existing registration methods.

Yan et al. used FEA of for quantifying organ motion based on volumetric meshes retrieved from segmentation of CT images. This was used for dose accumulation [6]. Ferrant et al. used active surfaces and distance fields for initial surface matching of brain meshes and FEA for subsequent computation of interior mesh vertex displacements [7]. This model was also used for prostate registration[8]. Brock et al. also use FEA for estimating interior vertex displacements after initial boundary vertex projections [9][10] and have also in earlier work used a linear elastic model for investigating the impact of breathing deformation on the delivered dose to a liver tumour[11]. They use a pre-computed surface correspondence map based on curvature correspondences as boundary conditions to the simulation.

Liang and Yan note that the accuracy of such techniques is limited by the surface projection algorithm [12]. To alleviate this problem they solve for interior and boundary vertices simultaneously by applying extra constraints ensuring that boundary vertices of the deforming organ stay on a triangle mesh describing the surface of the reference organ. Their model requires initial user defined boundary landmark correspondences.

In most work on FEM in image registration a linear elastic tissue deformation model has been applied. For large deformations however, especially those involving rotation, this model induces significant errors [13]. Consequently we have chosen a non-linear model.

Recently Choi et al. published an iterative mesh fitting method which bears many similarities with our method [14]. They define a surface distance term for driving the registration. Unlike our approach their method uses a linear elastic FEM to displace meshes. In order to handle large deformations they utilise a technique called stiffness warping to account for the rotational part of the deformation. Zhang et al. avoid manual definition of landmarks by employing a finite element contact impact analysis [15]. This allows a model of a lung to slide in the pleural cavity. They compute the deformation in multiple steps since their linear elastic model is not able to handle the large deformations of the lung in one step. Also Haker et al. use an iterative FEM [16]. Based on landmarks they project both source and reference organs onto a sphere using an active surface model. The sphere has been triangulated into a tetrahedral mesh, and guided by a few control landmarks, a point correspondence is found for mesh vertices. These are used as boundary conditions for a volumetric finite element analysis. Their work is based on theory in conformal mapping¹[17][18]. Conformal mapping was also used by Warfield et al., who also extended the linear elastic model with inhomogeneous material characteristics which allows fibres to be modelled [19].

Euclidean *distance fields* are used in an N -dimensional space to track the (Euclidean) distance to the closest point of an object in this space. In 3D the field is used to describe the distance to a 2D surface. Besides the already mentioned work by Ferrant et al. [7] and Choi et al. [14], a number of groups working on medical image registration have included the use of Euclidean distance fields in their work. In [20] tissue classification in reference CT images is performed based on fixed Hounsfield units and distance fields to material boundaries are computed. In the source image bones are represented as a point cloud. Based on an SSD measure of distance values bones are rigidly registered to the reference image. This is used for tracking of wrist bones. Marai et al. also minimised a cost function of distance field terms to recover rigid body transformations [20]. In [21] a similarity metric based on the sum of squared difference of distance fields is constructed for shape matching. Here the transformation consists of both a rigid term and a term for local deformable corrections. Xiao et al. use distance fields for rigid registration of surfaces that only partially overlap [22].

¹ That the mapping is conformal means that it is bijective and that angles are preserved.

3 Materials and Method

3.1 Mesh Representation

Our aim is to register a volume of interest (VOI), usually an organ, given at two different configurations. Data from a three-dimensional imaging source has been segmented prior to the registration and the VOI in both source and reference datasets are represented as binary volumes. These binary images are initially smoothed using a Gaussian filter. Next, Euclidean distance fields $\phi : \mathbb{R}^3 \rightarrow \mathbb{R}$ are generated for both datasets (Insight Segmentation and Registration Toolkit, ITK)².

Based on the distance fields we use an in-house implementation of the isosurface stuffing mesh generation algorithm [23] which produces a tetrahedral mesh. This meshing method guarantees strict upper and lower bounds on the dihedral angles in the generated tetrahedra, which increases the stability of the FEM.

3.2 External Driving Forces

The aim of the registration is to find a transformation of mesh nodes such that the surface nodes of the source body is mapped to the surface of the reference body while interior nodes are at an equilibrium. We propose an iterative algorithm driven by forces computed near the boundary of the source shape. These forces, concatenated in the vector \mathbf{R} , are defined for each source mesh node i by

$$\mathbf{R}_i = \gamma(\mathbf{A}_i + \beta\mathbf{B}_i) \quad (1)$$

where β is constant throughout the registration process and γ is iteratively increased until the surface match is achieved.

The force term \mathbf{A} is based on the distance fields that were pre-computed before mesh generation of both the source (ϕ_S) and reference (ϕ_R) VOI. It applies to all mesh nodes less than τ millimetres from the source shape surface and is given by

$$\mathbf{A}_i = (\phi_S(\mathbf{p}_i^o) - \phi_R(\mathbf{p}_i^d)) \nabla \phi_R|_{\mathbf{p}_i^d} \quad (2)$$

where \mathbf{p}_i^o denotes the initial position of particle i (in the source shape) and \mathbf{p}_i^d denotes the position of particle i in the current configuration of the iterative registration process. The expression $\phi_R|_{\mathbf{p}_i^d}$ evaluates the reference surface distance at the deformed position of particle i . Intuitively Eq. (2) provides force vectors in the direction of steepest descent of the distance field calculated from the reference shape - i.e. towards the reference volume. The forces are weighted with the difference between each particle's current distance to the reference shape and the particles original distance from the surface in the source shape. \mathbf{A}_i vanishes as particle i finds it "desired" distance to the reference surface.

² See <http://www.itk.org/>

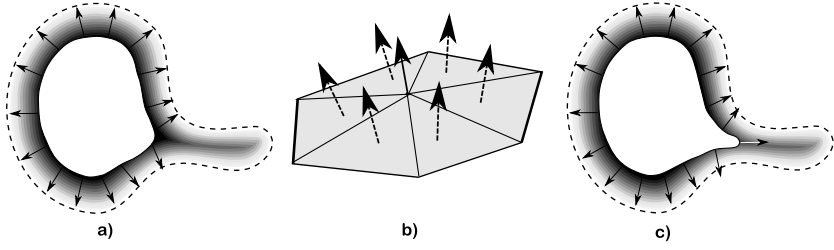


Fig. 1. Illustration of the forces driving the source shape surface vertices towards the surface of the reference shape. a) 2D illustration showing the reference surface (dashed line), distance field (intensity gradient), source shape (white area), and the direction of forces derived from force term **A**. b) a surface patch consisting of 6 surface triangles surrounding a vertex. A normal vector (dashed line) is calculated per triangle, and the mean vector is used in force term **B**. c) 2D illustration of **B** forces showing the same components as in a). Notice how this term allows the source boundary to move into narrow extrusions of the reference surface.

Force term **B** is working normal to the current configuration of the source surface and is calculated for all boundary nodes as the mean of all normal vectors from adjacent surface triangles:

$$\mathbf{B}_i = (\phi_S(\mathbf{p}_i^o) - \phi_R(\mathbf{p}_i^d)) \frac{1}{N_i} \sum_{\mathbf{f} \in \mathcal{T}_i} (\mathbf{f}_2 - \mathbf{f}_1) \times (\mathbf{f}_3 - \mathbf{f}_1) \quad (3)$$

where \mathcal{T}_i denotes the set of N_i surface triangles which include node i . Each surface triangle \mathbf{f} consists of node points \mathbf{f}_1 , \mathbf{f}_2 and \mathbf{f}_3 . The significance of force terms **A** and **B** is illustrated in fig. 1.

3.3 Non-linear Elastic Displacement

In each iteration a non-linear elastic FEM is used to displace the source mesh based on the "boundary" forces **R** computed above. This step is based on the work by Miller et al. defining a total Lagrangian explicit dynamics (TLED) FEM formulation [24]. An efficient parallel implementation have been described in detail by Taylor et. al [25]. A summary of their model is provided below.

The TLED FEM on a tetrahedral mesh leads to the standard equations of equilibrium, $\mathbf{M}\ddot{\mathbf{U}} + \mathbf{D}\dot{\mathbf{U}} + \mathbf{K}(\mathbf{U})\mathbf{U} = \mathbf{R}$, where \mathbf{U} is the nodal displacements, \mathbf{M} is a mass matrix, \mathbf{D} is a damping matrix, $\mathbf{K}(\mathbf{U})$ is a stiffness matrix, and \mathbf{R} is the external forces. Notice that \mathbf{K} is a function of \mathbf{U} . In this work we omit the dynamic terms $\mathbf{M}\ddot{\mathbf{U}}$ and $\mathbf{D}\dot{\mathbf{U}}$. Hence, for a given load of external forces we search for a configuration of nodal displacements \mathbf{U} in which $\mathbf{K}(\mathbf{U})\mathbf{U} = \mathbf{R}(\mathbf{U})$. In present work \mathbf{R} also depends on \mathbf{U} according to equations (1)-(3).

The TLED FEM method describes shape deformation and displacements with respect to the initial undeformed geometry. Element function derivatives precalculated from the initial mesh configuration are used in each iteration when calculating interior forces (stress and strain) reacting to an exterior load. I.e. with

such formulation continuous recalculation of spatial derivatives of the element functions is avoided. Deformation is measured in terms of the *deformation gradient* tensor ${}^t_0\mathbf{X}$ which contains elements ${}^t_0X_{ij} = \frac{\partial^t x_i}{\partial^0 x_j}$. In words, the deformation gradient describes the degree of displacement of material point coordinates ${}^t\mathbf{x}$ with respect to the initial position ${}^0\mathbf{x}$. By convention a left superscript describes at which configuration of the body a quantity is measured and left subscript describes the configuration the measurement is made with respect to. The deformation gradient can be calculated from the node displacements and precomputed element shape function derivatives [24], [25].

The internal forces $\mathbf{K}(\mathbf{U})\mathbf{U}$ are calculated as a sum of elemental forces $\mathbf{K}(\mathbf{U})\mathbf{U} = \mathbf{F}(\mathbf{U}) = \sum_e {}^t\tilde{\mathbf{F}}^{(e)}$ where e denotes the individual elements. For linear tetrahedral elements ${}^t\tilde{\mathbf{F}}$ can be evaluated as ${}^t\tilde{\mathbf{F}} = {}^0V {}^t_0\mathbf{B}_L^T {}^t\hat{\mathbf{S}}$ where 0V is the volume of the undeformed tetrahedron, ${}^0\mathbf{B}_L$ is the strain-displacement matrix, which describes the relationship between nodal displacements and strain in an element, and ${}^t\hat{\mathbf{S}} = [{}^t_0S_{11} {}^t_0S_{22} {}^t_0S_{33} {}^t_0S_{12} {}^t_0S_{23} {}^t_0S_{13}]^T$ is the second Piola-Kirchhoff stress on vector form. As the element deforms ${}^t_0\mathbf{B}_L$ can be found by transforming the initial strain displacement matrix ${}^0\mathbf{B}_{L0}$ using the transformation gradient : ${}^t_0\mathbf{B}_L^{(a)} = {}^0\mathbf{B}_{L0}^{(a)} {}^t_0\mathbf{X}^T$ [25]. For ${}^t\hat{\mathbf{S}}$ we use a hyperelastic neo-Hookean model given by ${}^t_0S_{ij} = \mu(\delta_{ij} - {}^t_0C_{ij}^{-1}) + \lambda^t J({}^tJ - 1){}^t_0C_{ij}^{-1}$. Here μ and λ are the Lamé constants, δ_{ij} is Kronecker's delta, ${}^tJ = \det({}^t_0\mathbf{X})$, and ${}^t_0\mathbf{C}$ is the Right Cauchy-Green deformation tensor calculated by ${}^t_0\mathbf{C} = {}^t_0\mathbf{X}^T {}^t_0\mathbf{X}$.

3.4 Registration Algorithm

The search for a source mesh deformation in which the source and reference surfaces are matched while interior nodes are at equilibrium is based on a gradient descent type approach. In each iteration of the registration algorithm the total forces, $\mathbf{T}(\mathbf{U})$, acting on the source shape is calculated as $\mathbf{T}(\mathbf{U}) = \mathbf{R}(\mathbf{U}) + \mathbf{F}(\mathbf{U})$. Each entry in this vector is used to update displacements ($\mathbf{U}_i \leftarrow \mathbf{U}_i + \delta \cdot \mathbf{T}_i$) with a maximum allowed displacement change of $\Delta_{U,max}$.

The scaling factor γ (Eq. (1)) is iteratively increased by multiplication with constant factor $\Delta_\gamma > 1$ whenever $\mathbf{T}(\mathbf{U})$ is approaching an equilibrium, i.e. when $\max(|\mathbf{T}(\mathbf{U})_i|) < T_1$. The algorithm terminates when all interior nodes are at rest and increasing γ does not increase $\max(|\mathbf{R}(\mathbf{U})_i|)$, at which point all surface nodes of the source mesh have been registered to the surface of the reference mesh. This leads to the termination criterion $\max(|\mathbf{T}(\mathbf{U})_i|) < T_2$.

3.5 Implementation

Compute intensive parts of the proposed registration method was implemented on the GPU using the programming framework CUDA. The GPU implementation of the TLED algorithm is similar to the implementation presented by Taylor et al. [25]. As the internal forces in the FEM are calculated per element the calculations in the TLED model can be massively parallelised. When accumulating forces from elementwise internal force computation, care must be taken

Algorithm 1. Overview of our registration algorithm

Let the source organ shape be represented as a tetrahedral mesh with original node distances $\phi_S(p_i^o)$ known
 Let the reference organ shape be represented as an Euclidean distance field ϕ_R
 Let β , τ , λ , and μ be known and constant
 Let all node displacements \mathbf{U} be initialised to zero
 $\gamma \leftarrow \gamma_0$
repeat
 Calculate external forces $\mathbf{R}(\mathbf{U})$ from (2), (3) and (1)
 Evaluate internal forces $\mathbf{F}(\mathbf{U})$ using the FEM
 Calculate resulting force $\mathbf{T}(\mathbf{U}) = \mathbf{R}(\mathbf{U}) + \mathbf{F}(\mathbf{U})$
 Update displacements $\mathbf{U}_i \leftarrow \mathbf{U}_i + \delta \cdot \mathbf{T}_i$, with a maximum displacement change of $\Delta_{U,max}$
 if $\max(|\mathbf{T}_i|) < T_1$ **then**
 $\gamma \leftarrow \gamma \cdot \Delta_\gamma$
until $\max(|\mathbf{T}_i|) < T_2$;

to avoid write conflicts. Our solution is to associate four write indices to each tetrahedron which enable us to know where to store the force contributions in elementwise kernels. A per-vertex kernel is subsequently responsible for addition of force contributions.

For evaluation of the expressions of the type $\max(|\mathbf{T}_i|) < T$, a kernel has been written which inspects a \mathbf{T}_i value and stores the value **false** in a fixed global memory position if $|\mathbf{T}_i| > T$. Before invocation of this kernel on all force vectors, **true** is written to the particular memory position, and if it is still **true** after all kernels have terminated the criterion $\max(|\mathbf{T}_i|) < T$ is fulfilled. The running times reported below are measured on an NVIDIA Quadro FX 5600 graphics card in a computer with an Intel core 2 6400 CPU.

3.6 Evaluation Data

Modelling wax phantom: To evaluate the performance of the proposed registration method when registering meshes undergoing large scale deformation, we constructed a phantom data set as a modelling wax cylinder. The phantom was CT-scanned in three configurations: **(a)** straight **(b)** bent approximately 45 degrees and **(c)** bent 90 degrees. The phantom surface was manually delineated. Seven lead markers were positioned on the surface of the phantom for evaluation purposes. The following parameters were used for the registration algorithm: $\beta = 0.01$, $\gamma_0 = 1000$, $\lambda = 5$ kPa, $\mu = 10$ kPa, $\Delta_\gamma = 1.03$, $\Delta_{U,max} = 0.005$ mm, $\tau = 5$ mm, $\delta = 0.01$, $T_1 = 30$ kN, and $T_2 = 3$ kN.

Prostate data set: To evaluate the algorithm on actual morphology acquired in vivo, we registered two manually delineated prostates from successive MRI scans of a prostate cancer patient. As no ground truth about the deformation between the two configurations **(a)** and **(b)** of the organ is available, an evaluation was performed based on inverse consistency of the resulting transformation. For

prostate registration parameters were set as above with the following exceptions: $\lambda = 0.33$ MPa, $\mu = 3.3$ kPa, and $\Delta_\gamma = 1.07$.

4 Results

4.1 Modelling Wax Phantom Registration

A mesh consisting of 6034 tetrahedra was constructed from configuration (a) of the phantom cylinder and registered to configurations (b) and (c). The two registrations were completed in 9 seconds and 17 seconds respectively. The results are shown in fig. 2. The marker positions were expressed in barycentric coordinates on a associated surface triangle and tracked to the final deformed configuration of the mesh. For each marker the registration error was calculated as the length of the difference vector between the registered marker position and the corresponding marker positions in the reference mesh. For the registration from configuration (a) to configuration (b) the initial error was $14.2 \text{ mm} \pm 12.7 \text{ mm}$ (average \pm std. dev.). After registration the error was reduced to $1.33 \text{ mm} \pm 1.39 \text{ mm}$. When registering configuration (a) to configuration (c) the error was reduced from $26.9 \text{ mm} \pm 24.8 \text{ mm}$ to $2.03 \text{ mm} \pm 1.03 \text{ mm}$.

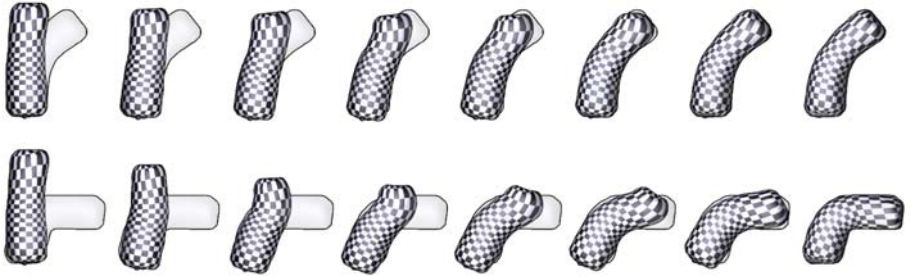


Fig. 2. Iterative registration of a modelling wax cylinder from a straight configuration to two configurations with different degrees of bending (top and bottom respectively). The leftmost images depict the initial source mesh configurations with the reference mesh overlaid transparently. The rightmost images depict the final deformation. Intermediate steps in between show every 1000th iteration (top) or every 2000th iteration (bottom). A checkerboard pattern has been mapped to the surface for visualisation of movement.

4.2 Prostate Registration

From the prostate delineations in two MRI dataset meshes were created consisting of 49005 (a) and 50697 (b) tetrahedra respectively. Two registrations were made: from (a) to (b) and (b) to (a). The running times of the two registration were 20 seconds and 28 seconds respectively. The results are shown in fig. 3. For

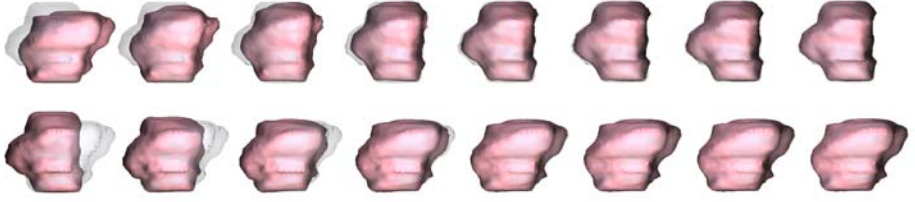


Fig. 3. Two-way registration of two prostate meshes obtained from successive MRI scans of a prostate cancer patient. The leftmost images depict the initial configurations of the source mesh with the reference mesh overlaid transparently. The rightmost images depict the final deformation. Intermediate steps in between show every 1000th iteration.

5000 randomly selected points inside prostate configuration **(a)** registration consistency errors were evaluated by transforming the point from configuration **(a)** to configuration **(b)** and back. The average inverse consistency errors were calculated as the average length of each vector between the initial and final points. The average obtained errors were $0.955 \text{ mm} \pm 0.469 \text{ mm}$ (max = 2.62 mm). This should be seen relative to the registration displacements of these same points: $6.25 \text{ mm} \pm 2.83 \text{ mm}$ (max = 16.4224 mm). The distribution of the inverse consistency errors can be seen in figure 4.

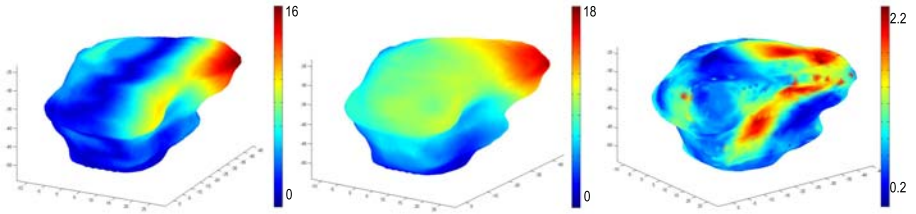


Fig. 4. Inverse consistency errors. Left: distance from source shape surface to surface of reference shape. Middle: Magnitude of deformation found by the registration. Right: Distribution of consistency errors 2 mm below surface. All measures are in millimetres.

5 Discussion

Considering the accumulation of inherent errors such as contouring errors, finite image resolution etc. we are satisfied with the accuracy achieved in the phantom experiment. With respect to the prostate registration we find a mean inverse consistency error of less than 1 mm promising as well. However, as the ground truth in the latter experiment is unknown, this does not necessarily imply that

the actual error is this low. Clinical studies including patients with implanted fiducial markers or other consistent anatomical landmarks within the VOI are needed to further evaluate the registration accuracy.

The proposed method includes a number of free parameters that must be defined initially. Based on our experience, the algorithm is quite robust with respect to the choice of most of these parameters. Note however that when different types of tissue are deformed, it is necessary not only to change the material parameters λ and μ but also to adjust Δ_γ which governs rate of increase the driving forces during the registration process.

By incorporating a physically consistent deformation model, it is possible to specify measured material properties for the morphology being registered. When using different parameters for e.g. tumour tissue and surrounding healthy tissue, we can furthermore register non-homogeneous materials. It is left for further studies to investigate this effect on the registration accuracy.

The introduction of the force term \mathbf{B} was motivated by the inability of the distance field term to lead the surface nodes into narrow boundary concavities. An alternative to introducing the \mathbf{B} term would be using the *gradient vector flow* approach of Xu and Prince [26]. Based on a diffusion of gradient vectors, their approach creates a vector field which points towards the surface but also points into narrow concavities.

Due to the nature of the proposed algorithm it can easily be parallelised and implemented e.g. on a GPU (as we did in this paper) to achieve high performance. We find that execution times in the order of 20-30 seconds very acceptable for potential clinical use. Due to the parameter $\Delta_{U,max}$, which limits the magnitude of displacement changes in each iteration, the running time is highly dependent on the initial magnitude of deformation between source and reference shapes. Thus registration times do vary from case to case.

Organ registration has multiple uses in the field of IGRT such as dose warping and dose accumulation. Importantly, since the proposed method relies on pre-segmented data, it can be used for multimodal registration of e.g. prostate in the context of functional imaging. Another potential use is creating patient-individual organ deformation models based on principal component analysis [27].

6 Conclusions

We have presented a method for finding point correspondences between organs delineated in successive scans. The method is based on Euclidean distance fields which allow us to evaluate local driving forces independently for each node in a tetrahedral mesh. The correspondence is regularised using a non-linear FEM. Driving force calculation and FEA is massively parallelisable allowing us to implement the method on a GPU. As a consequence the proposed method is very fast. It shows promise as a tool for use in IGRT and an important next step is a further examination of the achieved accuracy.

Acknowledgements

The work presented in this paper has been partly funded by Varian Medical Systems, Inc., Palo Alto, California and the Lundbeck Foundation Centre for Interventional Research in Radiation Oncology (CIRRO). Thanks to Kari Tanderup for the modelling wax phantom data and to Matthias Söhn for valuable discussions during the writing of this paper.

References

1. Noe, K.Ø., Mosegaard, J., Tanderup, K., Sørensen, T.S.: A framework for shape matching in deformable image registration. *Stud. Health. Technol. Inform.* 132, 333–335 (2008)
2. Marchal, M., Promayon, E., Troccaz, J.: Simulating prostate surgical procedures with a discrete soft tissue model. In: *Workshop in Virtual Reality and Physical Simulation* (2006)
3. Hagemann, A., Rohr, K., Stiehl, H.S., Spetzger, U., Gilsbach, J.M.: Biomechanical modeling of the human head for physically based, nonrigid image registration. *IEEE transactions on medical imaging* 18, 875–882 (1999)
4. Hagemann, A., Rohr, K., Stiehl, H.S.: Coupling of fluid and elastic models for biomechanical simulations of brain deformations using fem. *Medical Image Analysis* 6(4), 375–388 (2002)
5. Schnabel, J., Tanner, C., Castellano-Smith, A., Degenhard, A., Leach, M., Hose, D., Hill, D., Hawkes, D.: Validation of nonrigid image registration using finite-element methods: application to breast mr images. *IEEE Transactions on Medical Imaging* 22(2), 238–247 (2003)
6. Yan, D., Jaffray, D.A., Wong, J.W.: A model to accumulate fractionated dose in a deforming organ. *International Journal of Radiation Oncology*Biology*Physics* 44(3), 665–675 (1999)
7. Ferrant, M., Warfield, S.K., Nabavi, A., Jolesz, F.A., Kikinis, R.: Registration of 3d intraoperative mr images of the brain using a finite element biomechanical model. *IEEE Transactions on Medical Imaging*, 1384–1397 (2001)
8. Bharatha, A., Hirose, M., Hata, N., Warfield, S.K., Ferrant, M., Zou, K.H., Suarez-Santana, E., Ruiz-Alzola, J., D’Amico, A., Cormack, R.A., Kikinis, R., Jolesz, F.A., Tempany, C.M.C.: Evaluation of three-dimensional finite element-based deformable registration of pre- and intraoperative prostate imaging. *Medical Physics* 28, 2551–2560 (2001)
9. Brock, K.K., Sharpe, M.B., Dawson, L.A., Kim, S.M., Jaffray, D.A.: Accuracy of finite element model-based multi-organ deformable image registration. *Medical Physics* 32(6), 1647–1659 (2005)
10. Brock, K.K., Dawson, L.A., Sharpe, M.B., Moseley, D.J., Jaffray, D.A.: Feasibility of a novel deformable image registration technique to facilitate classification, targeting, and monitoring of tumor and normal tissue. *Int. J. Radiat. Oncol. Biol. Phys.* 64(4), 1245–1254 (2006)
11. Brock, K.K., McShan, D.L., Haken, R.K.T., Hollister, S.J., Dawson, L.A., Balter, J.M.: Inclusion of organ deformation in dose calculations. *Medical Physics* 30(3), 290–295 (2003)
12. Liang, J., Yan, D.: Reducing uncertainties in volumetric image based deformable organ registration. *Med. Phys.* 30, 2116–2122 (2003)

13. Picinbono, G., Delingette, H., Ayache, N.: Nonlinear and anisotropic elastic soft tissue models for medical simulation. In: Proceedings of IEEE International Conference on Robotics and Automation (ICRA), 2001, vol. 2, pp. 1370–1375 (2001)
14. Choi, J., Szymczak, A.: Fitting solid meshes to animated surfaces using linear elasticity. *ACM Trans. Graph.* 28(1), 1–10 (2009)
15. Zhang, T., Orton, N.P., Mackie, T.R., Paliwal, B.R.: Technical note: A novel boundary condition using contact elements for finite element based deformable image registration. *Medical Physics* 31(9), 2412–2415 (2004)
16. Haker, S., Warfield, S.K., Tempany, C.M.: Landmark-guided surface matching and volumetric warping for improved prostate biopsy targeting and guidance. In: Barillot, C., Haynor, D.R., Hellier, P. (eds.) MICCAI 2004. LNCS, vol. 3216, pp. 853–861. Springer, Heidelberg (2004)
17. Angenent, S., Haker, S., Tannenbaum, A., Kikinis, R.: On the laplace-beltrami operator and brain surface flattening. *IEEE Transactions on Medical Imaging* 18(8), 700–711 (1999)
18. Haker, S., Angenent, S., Tannenbaum, A., Kikinis, R., Sapiro, G., Halle, M.: Conformal surface parameterization for texture mapping. *IEEE Transactions on Visualization and Computer Graphics* 6(2), 181–189 (2000)
19. Warfield, S.K., Haker, S.J., Talos, I.F., Kemper, C.A., Weisenfeld, N., Mewes, A.U., Goldberg-Zimring, D., Zou, K.H., Westin, C.F., Wells, W.M., Tempany, C.M., Golby, A., Black, P.M., Jolesz, F.A., Kikinis, R.: Capturing intraoperative deformations: research experience at brigham and women’s hospital. *Medical Image Analysis* 9(2), 145–162 (2005)
20. Marai, G.E., Laidlaw, D.H., Crisco, J.J.: Super-resolution registration using tissue-classified distance fields. *IEEE transactions on medical imaging* 25, 177–187 (2006)
21. Paragios, N., Rousson, M., Ramesha, V.: Non-rigid registration using distance functions. In: *Computer Vision and Image Understanding*, pp. 142–165 (2003)
22. Xiao, G., Ong, S., Foong, K.: 3d registration of partially overlapping surfaces using a volumetric approach. *Image and Vision Computing* 25(6), 934–944 (2007)
23. Labelle, F., Shewchuk, J.R.: Isosurface stuffing: fast tetrahedral meshes with good dihedral angles. In: *SIGGRAPH 2007: ACM SIGGRAPH 2007 papers*, p. 57. ACM, New York (2007)
24. Miller, C., Joldes, G., Lance, D., Wittek, A.: Total lagrangian explicit dynamics finite element algorithm for computing soft tissue deformation. *Communications in Numerical Methods in Engineering* 23(2), 121–134 (2006)
25. Taylor, Z.A., Cheng, M., Ourselin, S.: High-speed nonlinear finite element analysis for surgical simulation using graphics processing units. *IEEE Transactions on Medical Imaging* 27(5), 650–663 (2008)
26. Xu, C., Prince, J.: Snakes, shapes, and gradient vector flow. *IEEE Transactions on Image Processing* 7(3), 359–369 (1998)
27. Söhn, M., Birkner, M., Yan, D., Alber, M.: Modelling individual geometric variation based on dominant eigenmodes of organ deformation: implementation and evaluation. *Physics in Medicine and Biology* 50, 5893–5908 (2005)